Therapeutic suppression of *Tubb4a* rescues H-ABC leukodystrophy.

Sunetra Sase[1*], Julia L Hacker[1*], Prabhat R. Napit[1], Sarah Woidill[1], Anjali Bhagavatula[1], Annemarie D'Alessandro[1], Akshata Almad[1], Asako Takanohashi[1], Quasar Padiath[2], Eric D. Marsh [1,2] and Adeline Vanderver[1,2]

*These authors contributed equally to this work

Correspondence to: Dr. Adeline Vanderver
Department of Neurology, The Children's Hospital of Philadelphia, Philadelphia, Pennsylvania, 19104, USA.
Email: vandervera@email.chop.edu

1 Division of Neurology, Department of Pediatrics, the Children's Hospital of Philadelphia, Philadelphia, Pennsylvania, USA.
2 Department of Neurology, Perelman School of Medicine, University of Pennsylvania, Philadelphia, Pennsylvania, USA.
3 Department of Human Genetics and Neurobiology, University of Pittsburgh, Pennsylvania, USA

Keywords: *TUBB4A*, microtubule, leukodystrophy, hypomyelination, anti-sense oligonucleotides

Running Title: A pre-clinical treatment development for H-ABC

Abstract

Hypomyelination and atrophy of basal ganglia and cerebellum (H-ABC) is a rare leukodystrophy associated with causal variants in β-tubulin 4A (*TUBB4A*). The recurring variant p.Asp249Asn (D249N) presents in infancy with dystonia, communication deficits, and loss of ambulation during the first decade of life. In this study, we characterized a genetic murine series (*Tubb4a*$^{KO/KO}$, *Tubb4a*$^{D249N/+}$, *Tubb4a*$^{D249N/KO,}$ and *Tubb4a*$^{D249N/D249N}$) to demonstrate that disease severity correlates with the expression of mutant Tubb4a and relative preservation of WT tubulin. To further evaluate the translational potential of *Tubb4a* suppression as a therapy in H-ABC, we identified a well-tolerated *Tubb4a*-targeted antisense oligonucleotide (ASO) candidate that selectively reduces Tubb4a *in vitro* and *in vivo*. Notably, single intracerebroventricular (i.c.v.) administration of ASO in postnatal *Tubb4a*$^{D249N/KO}$ mice drastically extends its lifespan, improves motor phenotypes, and reduces seizures. Neuropathologically, ASO treatment in *Tubb4a*$^{D249N/KO}$ mice restores myelin and oligodendrocyte survival. Furthermore, *in vivo* visual evoked potential latencies recover in ASO-treated *Tubb4a*$^{D249N/KO}$ mice. This is the first preclinical proof-of-concept for *Tubb4a* suppression via ASO as a disease-modifying therapy for H-ABC.

Introduction

TUBB4A-related leukodystrophy is a rare neurodevelopmental disorder associated with monoallelic pathogenic variants in the *TUBB4A* gene (1). These variants cause a heterogenous disease spectrum ranging from a severe early infantile encephalopathy, a late infantile presentation typified by progressive motor impairment, and a mild juvenile or adult-onset phenotype with prominent dystonia and spastic diplegia. The late infantile form is often defined by the characteristic neuroimaging features of hypomyelination and atrophy of basal ganglia and cerebellum (H-ABC) (2, 3). H-ABC is also closely associated with a single recurrent variant, p.Asp249Asn (D249N), present in over 20% of published individuals (4). H-ABC typically manifests in toddlers after normal development with progressive gait impairment and clinical features of spasticity, rigidity, dystonia, and cerebellar ataxia. Affected individuals experience feeding difficulties, seizures, loss of communication, and ambulation loss before the end of the first decade of life. No curative treatments are available for H-ABC; disease-modifying therapies are urgently needed (1-3, 5).

TUBB4A encodes the β-tubulin 4A protein, which is highly expressed in oligodendrocytes (OL; myelin-producing cells) and specific central nervous system (CNS) neurons (6, 7). β-tubulins such as TUBB4A heterodimerize with the α-tubulin to form microtubules (MT), which are highly dynamic polymers essential for the extension of OL processes, myelin sheath elongation, and neuronal growth, morphology, and migration (8, 9). *TUBB4A* mutations disrupt MT dynamics and polymerization, which may burden critical myelin and neuronal protein and organelle transport necessary for early neurodevelopment (10-12). H-ABC pathology demonstrates cell-autonomous deficits in OL lineage cells, striatal neurons (medium spiny neurons; MSNs), and cerebellar granule neurons (CGNs) (7, 13) corresponding to clinical and radiologic manifestations.

To model H-ABC, different *Tubb4a*-associated rodent models have been reported (10, 14, 15). Our own published H-ABC mouse model with homozygous D249N variants (*Tubb4a*$^{D249N/D249N}$) shows a severe phenotype with progressive ataxia, gait abnormalities, tremor, severe hypomyelination and significant loss of OLs, CGNs, and striatal neurons (humane end-stage at postnatal day [P32-37]) (10). A recent study reported a *Tubb4a* knockout (*Tubb4a*$^{KO/KO}$) mouse model with no behavioral or myelination deficits which is attributed to compensation by other tubulin monomers in MT assembly (14). This study using a mouse model with a different *Tubb4a* variant, *Tubb4a* p.Asn414Lys mutation ([N414K]; *Tubb4a*$^{N414K/+}$), also defined CGN and OL involvement as cell-autonomous (14). Studies of MT dynamics across published rodent and induced pluripotent cells (iPSCs) models show that mutant *Tubb4a* causes toxic gain-of-function,

disrupting MT polymerization and stability (10, 11, 14). Together, these findings support the idea that reducing toxic Tubb4a may be a valuable therapeutic strategy in *TUBB4A*-related leukodystrophy.

Targeted antisense oligonucleotides (ASOs) to reduce messenger RNA (mRNA) levels are in clinical use and provide promising clinical benefits in pediatric neurodegenerative diseases (16, 17). ASOs are short, single-stranded DNA molecules designed to degrade target mRNA and block translation of the encoded protein. ASO gapmer design chemistry is well-established and contains a phosphorothioate (PS) backbone with 2′-O-methoxyethyl (2′-MOE), and locked nucleic acid modifications (18). These ASO gapmers bind to target mRNA, resulting in RNase H1-mediated mRNA degradation.

The current study investigated the germline and therapeutic potential of reducing Tubb4a in our H-ABC mouse model. We characterized *Tubb4a*$^{KO/KO}$, and *Tubb4a*$^{D249N/KO}$ mice relative to wildtype (WT), *Tubb4a*$^{D249N/+}$, and *Tubb4a*$^{D249N/D249N}$ mice. The compound heterozygote model, *Tubb4a*$^{D249N/KO}$, displays severe deficits albeit with slower disease progression relative to *Tubb4a*$^{D249N/D249N}$ mice. We also confirmed that germline loss of *Tubb4a* is well-tolerated (14). To test the therapeutic potential of *Tubb4a* downregulation, we developed, screened, and selected anti-*Tubb4a* ASO. We show that administration of a *Tubb4a*-targeted ASO via intracerebroventricular injection (i.c.v.) bolus into postnatal *Tubb4a*$^{D249N/KO}$ mice remarkably lengthened survival, improved behavioral performance, decreased seizures and preserved myelin. A *Tubb4a* ASO-based therapy is the first molecular therapy for H-ABC and supports *Tubb4a* suppression approaches in clinical trials with potential applicability across the spectrum of *TUBB4A*-associated leukodystrophies.

Results

Germline suppression of *Tubb4a* and relative preservation of WT rescue D249N-associated motor phenotypes.

To confirm whether *Tubb4a* suppression provides a therapeutic benefit in H-ABC leukodystrophy, we bred H-ABC models *Tubb4a*$^{D249N/+}$ (10) and the *Tubb4a*$^{KO/+}$ mouse model (obtained from KOMP consortium) to create a phenotypic spectrum with a variable dosage of Tubb4a mutant and WT. The *Tubb4a*$^{D249N/+}$ mouse model exhibits myelin deficits without behavioral abnormalities and can reproduce. The *Tubb4a*$^{KO/+}$ mice are phenotypically normal and reproduce well. Their progeny includes *Tubb4a*$^{KO/KO}$, *Tubb4a*$^{D249N/KO}$ and *Tubb4a*$^{D249N/D249N}$ mice. As per published reports (14), *Tubb4a*$^{KO/KO}$ mice are viable and fertile, have no overt cage

behavior abnormalities or differences in weaning compared with WT littermates, and have normal survival (**Figure 1B**). The homozygous *Tubb4a*$^{D249N/D249N}$ mice mirror the cellular, molecular, and neurologic phenotypes (myelin loss and neuronal atrophy) of classical H-ABC (10). They show severe tremor, ataxia, and seizures (lasting > 30 seconds) starting at P7-P10 and reach a humane end-stage at P32-P37. The compound heterozygote mouse model *Tubb4a*$^{D249N/KO}$ exhibits an extended lifespan with later onset of tremors and ataxia (P21-P30) and later onset of severe dystonia and seizures close to the humane end-stage (mean survival=P108-P110). To determine the disease course, we conducted various motor neurobehavioral tests across all genotypes at different ages. Additionally, we quantified tremor, a common disease phenotype, by measuring tremor amplitudes at ages across all genotypes (**Figure 1C**). We extended motor assessments for less symptomatic genotypes to one year. As expected, *Tubb4a*$^{KO/KO}$ and *Tubb4a*$^{D249N/+}$ mice show no tremors or motor impairment up to a year of life (**Figure 1C-F, Supplemental Figure 1A-D**). Though *Tubb4a*$^{D249N/D249N}$ mice display intense tremors at P21, tremor amplitude significantly decreases at humane end-stage (P32-37) due to limited locomotion (**Figure 1C**). In contrast, *Tubb4a*$^{D249N/KO}$ mice show only mild ataxia at P19-P21 and tremors at P30. This tremor progressively increases at P60 and P90 (**Figure 1C**). We tested mice on an accelerating rotarod and grip strength across all genotypes as limited by survival (**Figure 1B**). While *Tubb4a*$^{D249N/D249N}$ mice exhibit poor rotarod and grip strength performance, *Tubb4a*$^{D249N/KO}$ mice initially perform like WT mice but progressively decline by P60 to P90 (**Figure 1D-F**).

As *Tubb4a*$^{D249N/D249N}$ and *Tubb4a*$^{D249N/KO}$ mice approach the disease end-stage (P32-P37 and P108-110, respectively), they exhibit multiple spontaneous tonic-clonic seizures with hindlimb extension. This seizure activity mirrors clinical presentations of H-ABC individuals exhibiting epilepsy. We counted seizures over three hours in both mouse models and observed increased seizures in both models, with the most significant frequency in *Tubb4a*$^{D249N/D249N}$ mice. Notably, *Tubb4a*$^{KO/KO}$ and *Tubb4a*$^{D249N/+}$ do not exhibit any seizures (**Figure 1G**). Overall, motor impairment, survival and seizures were proportional to dosage of mutant *Tubb4a* relative to WT Tubb4a (*Tubb4a*$^{D249N/D249N}$ > *Tubb4a*$^{D249N/KO}$ > *Tubb4a*$^{D249N/+}$ > *Tubb4a*$^{KO/KO}$ or WT mice).

Germline suppression of the Tubb4a mutant copy preserves myelin.

H-ABC-affected individuals demonstrate CNS hypomyelination (1). To investigate myelin deficits in mice with variable *Tubb4a*^{D249N} dosage, we quantified Eriochrome Cyanine (Eri-C) staining and myelin basic protein (MBP) fluorescent signal of the MBP immunofluorescent staining, a marker for mature myelin sheaths at different disease. *Tubb4a*$^{KO/KO}$ and *Tubb4a*$^{D249N/+}$ mice display myelin sheaths (Eri-C and MBP signal) equivalent to WT in the corpus callosum and

cerebellum at all ages (**Figure 1H; Supplemental Figure 2-3).** In contrast to the sparse staining and reduced MBP in *Tubb4a*$^{D249N/D249N}$ mice at P21 and P32-P37 (end-stage of *Tubb4a*$^{D249N/D249N}$ mice), *Tubb4a*$^{D249N/KO}$ mice show moderate myelin (Eri-C) loss with intact MBP sheaths at P21. Nevertheless, there is progressive myelin degeneration (Eri-C and MBP staining) in these mice at P32-P37, P60, and end-stage in both corpus callosum and cerebellum (P108-P110) that becomes like end-stage *Tubb4a*$^{D249N/D249N}$ mice over time (**Figure 1H; Supplemental Figure 2-3**).

To get more detailed measures of the ultrastructural complexity of myelin, we carried out electron microscopy (EM) of the optic nerve and corpus callosum at P32-P37 (end-stage of *Tubb4a*$^{D249N/D249N}$ mice) and P108-P110 (end-stage of *Tubb4a*$^{D249N/KO}$ mice). We calculated the % of unmyelinated axons and g-ratio, a measure of myelin thickness (19). *Tubb4a*$^{KO/KO}$ mice exhibit well-defined and compact myelinated axons in both these areas as WT **(Figure 1H-J, Supplemental Figure 4**). *Tubb4a*$^{D249N/+}$ mice exhibit an increase in g-ratio, confirming mild myelin deficits in both regions (10) (**Figure 1H-J, Supplemental Figure 4 [Optic nerve]**). *Tubb4a*$^{D249N/KO}$ mice at P32-P37 exhibit a higher % of unmyelinated axons, and most of the axons show poor compaction (**Supplemental Figure 5**). Also, by end-stage (P108-P110), most of this myelin degenerates with an increase in the number of unmyelinated axons and g-ratio (**Figure 1H-J, Supplemental Figure 4**); however never as severe as that seen in end-stage *Tubb4a*$^{D249N/D249N}$ mice. *Tubb4a*$^{D249N/D249N}$ mutants show early and severe myelin loss as compared to all other genotypes, and the existing lower % of myelin sheaths are inappropriately thin for their axonal caliber (**Figure 1H-J, Supplemental Figure 4**). Along with copious amounts of myelin degeneration, both *Tubb4a*$^{D249N/D249N}$ and *Tubb4a*$^{D249N/KO}$ mice have increased microglia and macrophages conditioning myelin debris and vacuoles at end-stage (**Figure 1H-I, Supplemental Figures 4 and 5**).

Together, these results suggest that reducing the dosage of mutant *Tubb4a* and relatively preserving the WT copy delays and attenuates disease phenotype, supporting a toxic gain-of-function pathology for the D249N mutation in *TUBB4A*.

Germline suppression of the Tubb4a mutant copy mitigates cellular pathology.

We have previously reported that *Tubb4a*$^{D249N/D249N}$ mice show drastic OLs loss, which are myelin-producing cells (10); we quantified the total number of ASPA (a mature oligodendrocyte marker) cells per mm^2 to Olig2$^+$ (an oligodendrocyte lineage marker) cells across all genotypes in the corpus callosum, cerebellar white matter and granule layer at different ages. OLs and Olig2+ cells are well preserved in *Tubb4a*$^{KO/KO}$ and *Tubb4a*$^{D249N/+}$ mice compared to WT mice in these

areas (**Figure 2A-D, Supplemental Figure 6)**. In the corpus callosum, *Tubb4a*$^{D249N/D249N}$ and *Tubb4a*$^{D249N/KO}$ mice demonstrate a significant reduction of ASPA+ cells at P21 and end-stage (P32-P37 and P108-P110, respectively) relative to WT mice (**Figure 2A-B, Supplemental Figure 6A**). We noted similar findings and loss of OLs in the cerebellar white matter and granule layers in these mutant models at their respective end-stages (**Figure 2A, Figure 2C-D**, and **Supplemental Figure 6B)**. Olig2+ cell numbers are comparable across all these genotypes (**Supplemental Figure 6**), suggesting overall OL lineage cells are preserved despite maturation deficits.

In various leukodystrophies, astrocytes and microglia promptly react to injury, activating astroglia (astrogliosis) and microglia (microgliosis). We carried out GFAP (astrogliosis) and Iba1 (microgliosis) immunostaining at P32-P37 and P108-P110 ages. Astrocytes and microglia are like WT littermates in *Tubb4a*$^{KO/KO}$ and *Tubb4a*$^{D249N/+}$ mice, whereas *Tubb4a*$^{D249N/D249N}$ and *Tubb4a*$^{D249N/KO}$ mice show elevated GFAP and Iba1 density in the corpus callosum and cerebellum (**Figure 2E**, **Supplemental Figures 7-9**).

Germline suppression of the Tubb4a mutant copy ameliorates neuronal pathology.

One of the most striking neurologic phenotypes in H-ABC-affected individuals is cerebellar and basal ganglia atrophy (1). CGNs constitute the bulk of cerebellar mass (20). As CGNs exhibit apoptotic death in *Tubb4a*$^{D249N/D249N}$ mutant mice (10), we estimated CGNs and their cell death by co-immunostaining of NeuN (a neuronal cell marker) and Caspase 3 (an apoptotic cell death marker) in all genotypes across different ages (**Figure 3A**). As expected, *Tubb4a*$^{KO/KO}$ and *Tubb4a*$^{D249N/+}$ mice do not experience neuronal loss or cell death (**Figure 3B-E, Supplemental Figure 10B**). In contrast, there is drastic death in *Tubb4a*$^{D249N/D249N}$ mice at P32-P37 (10). *Tubb4a*$^{D249N/KO}$ mice exhibit delay and mild neuronal loss and apoptosis, which is evident at P60 to humane end-stage (P108-P110; **Figure 3B-E, Supplemental Figure 10B**).

To assess if the reduction in D249N mutant copies mitigates the basal ganglia phenotype, we estimated the number of striatal neurons at P32-P37 and P108-P110 across all genotypes by immunofluorescent staining of NeuN and CTIP2 antibodies. CTIP2, a medium spiny neuronal marker, denotes striatal neurons, the neuronal population with the highest deficit in H-ABC-affected individuals (21) (5). Notably, no striatal neuron (CTIP2+) loss is evident in *Tubb4a*$^{KO/KO}$ and *Tubb4a*$^{D249N/+}$ mice (**Figure 3F-G, Supplemental Figure 10C-E**). *Tubb4a*$^{D249N/D249N}$ mice at end-stage (P32-P37) show a reduction of CTIP2+ and all striatal neurons (NeuN; **Figure 3F-G**, and **Supplemental Figure 10C-E**). *Tubb4a*$^{D249N/KO}$ mice exhibit a trend of decreased striatal

neurons at the end-stage (P108-P110), though the loss is insignificant (**Figure 3F-G, Supplemental Figure 10C-E**).

Spatial *Tubb4a* transcripts demonstrate robust expression in H-ABC-relevant brain areas.

To understand the spatial-temporal expression of *Tubb4a* mRNA at different ages, we performed RNAscope *in situ* hybridization at P0, P7, P14, P21, P32-P35, P108-P110 in WT and *Tubb4a*$^{KO/KO}$ sagittal brain sections. The mouse *Tubb4a* probe was specific as no signal was detected in the *Tubb4a*$^{KO/KO}$ brain sections (**Supplemental Figure 11**).

Within the forebrain, at P0, a few weakly stained *Tubb4a* cytoplasmic puncta are in cells within the cortical layers, striatum, and corpus callosum (**Figures 4A-E**). At P7 in cortical layers, we observe *Tubb4a* transcripts localized to layer I, but eventually, by P14, most of the cortical layers show an even transcript distribution (**Figure 4I, 4K and Supplemental Figure 12B**). All ages in the corpus callosum have *Tubb4a* transcripts in cells resembling oligodendrocyte lineage cells (**Figure 4, See Corpus callosum [CC] and Supplemental Figure 12**). All transcripts increase from P7 to P21 in different brain areas with stable *Tubb4a* expression patterns at P35 and P110 (**Figure 4, Supplemental Figures 11 and 12**), suggesting a critical *Tubb4a* role in the early neurodevelopmental phase.

Similarly, we examined cerebellar white matter and neuronal layers for *Tubb4a* transcripts across ages. In the cerebellar white matter, from age P7, the pattern of *Tubb4a* expression is similar in time course to that seen in the corpus callosum (**Figure 4F-G, 4M-N, and 4T-U, Supplemental Figure 12F-G, 12M-N, and 12T-U**). The cerebellar granule layer (CGL) comprises multiple cell types, including a large volume of CGNs, Golgi cells, Bergmann glia, and OL lineage cells. At P0, the CGL resides externally and has not migrated yet (22). In this non-migrated external layer, we note a few early cytoplasmic *Tubb4a* puncta at P0 (**Figure 4F-G**). Over time, these also increase from P7-P21 and achieve stable expression at later time points (**Figure 4M-N and 4T-U, Supplemental Figure 12F-G, 12M-N and 12T-U**).

Anti-sense administration reduces Tubb4a *in vitro* with minimal toxicity.

Given that germline *Tubb4a* reduction is well-tolerated, we sought to explore the translational potential of lowering Tubb4a levels using ASOs. Given that *Tubb4a* expression is present throughout development, we proposed early treatment. We designed a series of ASO candidates bound to mouse *Tubb4a* (coding regions). All ASOs included in the initial screen contained a 2'MOE modification with a phosphorothioate (PS) backbone, characteristics that are known for stability and low cytotoxicity (23, 24). ASO design included gapmers with complete PS

bonds or reduced PS bonds to reduce ASO-associated toxicity (23) (ASO designs are provided in **Supplemental Table 1**).

ASOs were screened in WT mouse cortical neurons *in vitro* by free uptake (gymnosis), followed by analysis of *Tubb4a* transcripts with qRT-PCR. To determine *in vitro* ASO toxicity, we carried out the ApoTox-Glo Triplex assay, which detects viability, cytotoxicity, and caspase activation events within a single well. We identified and selected candidate ASOs (8 ASO candidates) that efficiently decrease Tubb4a (>80%) at 5μM (*Tubb4a* downregulation of selected potential ASOs are in **Table 1,** and others are in **Supplemental Table 2**).

Tubb4a ASO 18-3 administration *in vivo* via i.c.v route exhibits maximum potency with minimal toxicity.

To investigate ASO toxicity and efficacy *in vivo*, we injected selected ASOs (8 ASO candidates) at a 15μg/g dose via an i.c.v. route in WT mice at P1 alongside vehicle-treated animals that received 2μL sterile PBS. Pups injected with ASO candidates 4, 6, and 7 died within 3-4 hours post-injection, which was attributed to acute neurotoxicity (25) (**Supplemental Table 3**). To explore the chronic neurotoxicity and off-target effects of the remaining ASO candidates (ASO 7-2, ASO 7-3, ASO 8-3, ASO 18-1, and ASO 18-3), we monitored mice weekly with a functional observational battery (FOB) at P30 (30 days post-injection). FOB is a well-established paradigm for quantifying behavioral neurotoxicity (26). WT mice injected with ASO 7-2 and ASO 18-1 demonstrate mild to severe neurologic deficits, including poor posture, ataxia, poor hindlimb grasp, and hyperactivity (**Supplemental Table 4**). WT mice injected with ASO 7-3 and ASO 8-3 display mild gait deficits, weight loss, and poor motor coordination by rotarod (**Supplemental Table 4, Supplemental Figure 13A**). Out of our 8 ASO candidates, we observed WT mice injected with ASO 18-3 perform similar to PBS-injected controls on neurobehavioral battery and rotarod tests (**Supplemental Table 4, Supplemental Figure 13 A and C**). Despite mild motor deficits observed in ASO 7-3 and ASO 8-3, we also assessed their *Tubb4a* downregulation to quantify the difference in efficacy with our promising ASO 18-3 candidate. After neurobehavioral assays were complete, we dissected and isolated different brain tissues (cortex, cerebellum, and striatum) 30 days after ASO injection and performed qRT-PCR to determine *Tubb4a* expression levels. All three ASO candidates showed similar *Tubb4a* downregulation potential but given that ASO 18-3 demonstrated a more reliable safety profile at 15μg/g dose, ASO 18-3 was selected for future experiments **(Supplemental Figure 13B**).

Administration of Tubb4a ASO 18-3 results in dose-dependent, long-lasting, and specific decreases of Tubb4a in WT and *Tubb4a*$^{D249N/KO}$ mice.

To determine the dose-dependent *in vivo* safety profile and *Tubb4a* downregulation potential of ASO 18-3, we performed i.c.v. injections of ASO 18-3 at P1 in WT mice with different doses (5,15, 20, and 30µg/g, n=4 mice per dose) alongside vehicle-treated (PBS) animals. We observed these mice weekly and noted the dose-associated lethality at 30µg/g of dose (75% of mice died within a few days post-injection). Analysis of mice's FOB and motor behavioral assays at 15, 20 and 30 µg/g doses at P30 show typical neurologic scores compared to PBS-injected controls (**Supplemental Figure 13C**).

To assess dose-dependent *Tubb4a* downregulation, we dissected and isolated different brain areas at P30 and determined the *Tubb4a* mRNA levels relative to PBS-injected controls using qRT-PCR. The administration of *Tubb4a* ASO 18-3 produced a dose-dependent knockdown of *Tubb4a* mRNA in the cortex and striatum with no significant downregulation in the cerebellum (**Figure 5B and Supplemental Figure 14A-B**). Tubb4a protein levels analyzed using immunoblotting at the 20µg/g dose match mRNA expression at P30 (**Figure 5B-C**; Tubb4a antibody specificity assessed with *Tubb4a*$^{KO/KO}$ brain tissue; **Supplemental Figure 14C**).

To assess the persistence of *Tubb4a* downregulation longitudinally, we conducted i.c.v. ASO injections at P1 at 20µg/g in WT mice and collected tissues at P30, P60, P90, and P160. We evaluated both *Tubb4a* mRNA and protein levels in the cortex, striatum, and cerebellum at these ages using qRT-PCR and western blot. We noted significant Tubb4a downregulation until P60; however, Tubb4a levels returned to normal at P90 and P160, suggesting that ASO 18-3 is effective for ~8-9 weeks (**Figure 5D-F**). Similarly, qRT-PCR showed significant *Tubb4a* downregulation in the cortex, striatum, and cerebellum in *Tubb4a*$^{D249N/KO}$ mice (**Figure 5G**). Of note, we did not analyze the Tubb4a protein downregulation in *Tubb4a*$^{D249N/KO}$ mice as the Tubb4a protein is downregulated in mutant mice relative to WT (**Supplemental Figure 14C**).

OLs, cortical, and striatal neurons show robust Tubb4a 18-3 ASO uptake.

To investigate spatial ASO uptake in different brain cells and areas, we generated fluorescently labeled Tubb4a ASO 18-3 using fluorescein amidites (FAM). FAM-tagged ASO 18-3 at 20µg/g in postnatal WT mice via i.c.v injection showed 100% lethality due to a suspected synergetic toxicity effect between ASO and FAM. Thus, we reduced the FAM-ASO dosing to 10µg/g and conducted i.c.v. injection in pups. This dose was well-tolerated in all pups and was used to evaluate further ASO distribution in different brain regions (the corpus callosum, cortex, striatum, and cerebellum).

We observed robust ASO distribution in the forebrain (**Figure 5H**) close to the lateral ventricles, cortex, corpus callosum, and striatum. The cerebellum shows minimal to moderate ASO uptake with no fluorescent signal in the granule layers (**Supplemental Figure 15**). To assess the ASO distribution in OL lineage cells, we carried out co-staining of CC1 (a mature oligodendrocyte marker) with FAM and NG2 (an oligodendrocyte precursor cells (OPC) marker) with FAM. We noted robust ASO uptake in OPCs and OLs in the corpus callosum, cortex, and striatum (**Figure 5I-J**, **Supplemental Figures 16-19**). Cerebellar white matter displays ASO uptake in OLs but is less robust than the corpus callosum (**Supplemental Figures 17B**). We also co-stained NeuN (a neuronal marker) and FAM to assess ASO uptake in neurons. We observed ASO distribution in cortical and striatal neurons with no significant ASO uptake in CGNs (**Figure 5J**, **Supplemental Figures 20 and 21**).

ASO-improved motor function and survival in *Tubb4a*$^{D249N/KO}$ mice.

We next evaluated if a single i.c.v. injection of ASO candidate 18-3 efficiently rescues motor phenotypes and improves survival in postnatal *Tubb4a*$^{D249N/KO}$ mice (P1-2) (Study design, **Figure 6A**). Remarkably, *Tubb4a*$^{D249N/KO}$ mice injected with Tubb4a ASO 18-3 show greatly expanded survival (**Figure 6B**, Mean survival = P365-P370) compared to PBS-injected *Tubb4a*$^{D249N/KO}$ mice (Mean survival= P108-P110). We conducted accelerating rotarod, grip strength, and tremor assays to determine whether ASO 18-3 could improve motor function in *Tubb4a*$^{D249N/KO}$ mice. Tubb4a ASO-treated *Tubb4a*$^{D249N/KO}$ mice display remarkable rotarod performance relative to untreated mice until P120, suggesting improved balance and coordination (**Figure 6C, Videos 1 and 2** shows improved phenotype in treated *Tubb4a*$^{D249N/KO}$ mice versus untreated *Tubb4a*$^{D249N/KO}$ mice). Their grip strength and tremor assay performance further substantiate these improvements (**Figure 6D-F)**. However, the motor function in ASO-treated *Tubb4a* mutants starts to decline after P90, corresponding to a decrease in ASO efficacy and return to baseline of Tubb4a expression between 60-90 days after a single i.c.v. injection of ASO (**Figure 5D-F**). Of note, because untreated *Tubb4a*$^{D249N/KO}$ mice die at P108-P110, the surviving ASO-treated *Tubb4a*$^{D249N/KO}$ mice were measured against WT untreated and ASO-treated mice. Importantly, even after rotarod performance declines, Tubb4a ASO-treated *Tubb4a*$^{D249N/KO}$ mice continue to stay mobile until P250 in open-field testing and perform equivalently to WT PBS-treated mice (**Figure 6G-H)**. However, this activity drops at P300 (close to their end-stage). This data suggests that ASO 18-3 treatment delays the onset of motor deficits in H-ABC mice while the ASO effect is ongoing. Of note, both Tubb4a ASO-treated *Tubb4a*$^{D249N/KO}$ and WT ASO-treated mice exhibit an increase in their exploratory activity relative to PBS-treated WT mice

without changes in freezing % (data not shown) and average speed (**Figure 6H** and **Supplemental Figure 22A).** Increased exploratory activity is often thought to be correlated with anxiety. However, this behavior in association with ASO treatment is of unknown cause. Notably, our mice also have generalized astrogliosis (increase in *Gfap* transcripts via Nanostring; (**Supplemental Figure 30**), which is also linked with increased exploratory activity (27).

ASO-mediated suppression of Tubb4a effectively restores functional myelin and OLs

To assess myelination and corresponding OL pathology after ASO 18-3 treatment, we quantified myelin using *Mbp* transcripts and MBP protein, Eri-C staining, and electron microscopy in different brain areas. *Mbp* transcripts (detected by Nanostring panel) and MBP protein are significantly restored in ASO-treated *Tubb4a*$^{D249N/KO}$ mice in the striatum and cortex (**Figure 6I-J, Supplemental Figure 22B-C and Supplemental Figure 30 for *Mbp* Nanostring**). We used electron microscopy to measure g-ratio and % unmyelinated axons in the corpus callosum and optic nerve across all treatment groups. ASO-treated *Tubb4a*$^{D249N/KO}$ mice show an increase in myelination in both areas relative to untreated *Tubb4a*$^{D249N/KO}$ mice as measured by g-ratio and % unmyelinated axons (**Figure 7B-D, Supplemental Figure 23)**. Of note, myelin in treated *Tubb4a*$^{D249N/KO}$ mice is still not as compact as in untreated WT mice. Additionally, at higher resolution at ~P110, myelin vacuolization improves in treated mice relative to untreated *Tubb4a*$^{D249N/KO}$ mice (**Figure 7E and Supplemental Figures 23E and 24**). We also noted a decrease in microglia and/or macrophages containing myelin debris in treated *Tubb4a*$^{D249N/KO}$ mice relative to untreated mutant mice **(Figure 7B and Supplemental Figure 24**). Similarly, myelin levels (Eri-C analysis) enhanced in ASO-treated *Tubb4a*$^{D249N/KO}$ mice relative to PBS-treated *Tubb4a*$^{D249N/KO}$ mice in the corpus callosum, striatum, and cerebellar white matter (**Figure 7F and 7J**, **Supplemental Figure 25, Supplemental Figure 26**); this effect is persistent in forebrain but not cerebellum through one year without additional ASO dosing (**Supplemental Figures 25 and 26**). Concordantly, ASO treatment restores mature OLs in treated H-ABC mice (corpus callosum at P48 and P108-P110) in contrast to their substantial depletion in untreated *Tubb4a*$^{D249N/KO}$ mice (**Figure 7I and 7J**). Importantly, there is a decrease in likely compensatory OPC proliferation at P48 in ASO-treated animals relative to untreated *Tubb4a*$^{D249N/KO}$ mice (**Supplemental Figure 27B-C**).

ASO-mediated suppression of Tubb4a restores the electrophysiological response.

To determine if the restored myelin is functional, we implanted 250um electrodes over the visual cortex through the skull. Visual evoked potentials (VEPs) are used to functionally assess visual

pathways and can be used as a biomarker of remyelination (28). We measured the N1, N2, P1, and P2 latencies and amplitudes of the VEPs (**Figure 7G and 7K-L**). We observed a delay in N1 latency in untreated *Tubb4a*$^{D249N/KO}$ mice compared to PBS-injected WT and ASO-treated WT mice. Notably, N1 latencies but not N1 amplitudes are significantly restored in ASO-treated *Tubb4a*$^{D249N/KO}$ mice at P48, suggesting that preserved myelin is functional at this age (**Figure 7G and 7K, Supplemental Figure 28 and 29A**). Interestingly, in untreated *Tubb4a*$^{D249N/KO}$ mice, a P2 peak appears to be shifted, and the P2 latencies are delayed (**Figure 7L**). ASO treatment restores P2 latencies in *Tubb4a*$^{D249N/KO}$ mice (**Figure 7G and 7L**).

Tubb4a ASO suppression fails to reverse cerebellar granule neuron (CGN) death and loss and leads to mild neuroinflammation.

Since the death of CGNs is a cell-autonomous deficit in H-ABC (14), we assessed whether ASO-treated *Tubb4a*$^{D249N/KO}$ mice show any evidence of cerebellar neuronal rescue. We co-stained CGN using NeuN (a neuronal marker) and caspase 3 (an apoptotic cell death marker) to assess cell death and cell numbers. We failed to see rescue at P48 of CGN cell death and cell numbers in treated *Tubb4a*$^{D249N/KO}$ mice (**Supplemental Figure 31**).

We performed Nanostring to evaluate whether ASO treatment rescues astrocyte activation, commonly seen in the *Tubb4a* mutant model. Unexpectedly, ASO causes astrogliosis in the cortex, striatum, and cerebellum of ASO-treated WT and *Tubb4a*$^{D249N/KO}$ *mice*. However, this may be specific to this candidate ASO and may not be related to *Tubb4a* suppression since no similar effect was seen in untreated *Tubb4a*$^{KO/KO}$ mice (**Supplemental Figure 30)**.

Discussion

There is an unmet need for effective treatment strategies for individuals affected by *TUBB4A*-associated disorder. This disorder includes a broad spectrum of phenotypes: early infantile encephalopathy, late infantile motor phenotypes including H-ABC, and adult-onset dystonia. A recurring D249N pathologic variant in *TUBB4A* is frequently present in H-ABC, which is characterized by progressive loss of neurologic skills in early childhood and eventual death. *Tubb4a*$^{D249N/KO}$ mice exhibit mild ataxia early (from P18-P21) with progressive worsening of motor function until their humane end-stage at P108-P110. Although motor deficits are not apparent during the juvenile phase (P21-P30), these mice show early myelination deficits at P21. Furthermore, the disease pathology is not restricted to OL lineage cells but extends to the loss of cerebellar granule neurons beginning at P48. The slower disease progression in *Tubb4a*$^{D249N/KO}$ mice makes these ideal for testing *TUBB4A*-related therapeutics.

This study assessed the germline and therapeutic efficacy of Tubb4a suppression. We characterized the *Tubb4a*$^{D249N/KO}$ mouse model, which mirrors severe H-ABC manifestations with slower disease progression. Importantly, a single i.c.v. injection using Tubb4a targeted ASO in *Tubb4a*$^{D249N/KO}$ mice successfully improved survival, motor phenotypes, and myelination deficits. Our study highlights that even a single ASO injection in this disease model can elicit a sustained phenotypic improvement relative to untreated cohorts, even with ~10-20% of myelin restoration. Importantly, we also noted that ASO treatment restores *Mbp* transcripts in the treated H-ABC mice. In OLs, *Mbp* mRNA granules are transported via microtubules and translated locally in OL processes, suggesting the restoration of transport mechanisms after ASO treatment (29, 30). We see a dramatic improvement in cellular, evoked potential latencies, and functional measures in the ASO-treated mouse model. For visual evoked potential response in H-ABC mice, we see a hyperresponsive N1 peak relative to WT controls. This may be related to the primary auditory cortex or a lack of surround inhibition in the cortex, giving a large response. Interestingly, auditory impairment occurs in the H-ABC (31). Notably, treated H-ABC mice exhibit improvement in P2 latencies relative to untreated mice. P2 latencies represent GABA-mediated inhibition (32). Notably, this Tubb4a anti-sense therapy is not specific to the recurring D249N variant and is well-suited for broader applications in *TUBB4A*-associated leukodystrophy. Recent data suggests that germline deletion of *Tubb4a* in rodents recruits other tubulins, resulting in no abnormal phenotype (14). More studies are needed to investigate how ASO mediates and changes the β-tubulin composition.

H-ABC leukodystrophy involves cell-autonomous deficits in OLs, CGNs, and striatal neurons, making it challenging to develop a treatment targeting all these cell types. Our spatial data suggests that ASOs are well-distributed in OLs, cortical, and striatal neurons but fail to target CGNs. This may limit the efficacy of ASO-based therapeutics in this disorder. However, we see substantial therapeutic effects in our mice with even a single administration that primarily restores myelination. Thus, even partial cellular rescue in H-ABC may result in significant clinical benefit while therapies that more globally target affected cells are developed.

Several important questions remain, including whether repeated ASO treatments will lead to prolonged improvement in pre-symptomatic mice. Future work will require determining the best dosing route, frequency, and detailed characterization of ASO pharmacokinetic and pharmacodynamic properties within the CNS. In addition, ASO 18-3 treated mice showed astrogliosis and microgliosis, which suggest an activated immune response in the brain. The FAM-labeled 18-3 ASO was injected at lower dosing (10μg/g) and showed robust OLs distribution; it remains to be assessed if we can reduce ASO dosing or if other ASO designs can demonstrate

similar disease mitigation with no astrogliosis or microgliosis. Finally, additional models of milder and more severe *TUBB4A*-associated leukodystrophy, with other pathogenic variants, would help establish the generalizability of these findings.

Overall, Tubb4a ASO treatment leads to efficacious Tubb4a downregulation in H-ABC mouse models. Our study demonstrates that despite failing to target CGNs, ASO treatment preserves myelination, improves motor and functional outcomes, and reverses many aspects of the disease phenotype. We believe that Tubb4a ASOs are a promising therapeutic strategy in H-ABC and *TUBB4A*-associated leukodystrophy.

Methods:

Animals. All animal protocols were approved by the Institutional Animal Care and Use Committee (IACUC) at the Children's Hospital of Philadelphia. Equal number of females and males are included in this study. All mice were generated on the C57/BL6J background. *Tubb4a*$^{KO/+}$ mice (KOMP consortium) were intercrossed to obtain *Tubb4a*$^{KO/KO}$. *Tubb4a*$^{KO/+}$ model was crossed with *Tubb4a*$^{D249N/+}$ to obtain *Tubb4a*$^{D249N/KO}$ mice. F1 litters were used for experiments. All animals were maintained in a temperature-controlled room, with a 12-hour light on/off cycle and free access to food and liquid. For genotyping, tail snips were collected and outsourced to TransnetYX, Inc (Cordoba, TN).

Oligonucleotides design and synthesis. The ASO library was designed against the full mouse Tubb4a mRNA sequence. After ASO *in silico* modeling, the number of phosphorothioate bonds were modified to reduce potential toxicity and obtain multiple designs from the parent molecule. All ASOs were synthesized at BioSpring (BioSpring, Germany) and suspended in aliquots containing Phosphate buffer saline (PBS; Thermo Scientific, 1001-023) and then stored at -20 or -80°C.

In vitro ASO screening. ASO *in vitro* screening was carried out using primary mouse cortical neurons. Embryos were removed at E15.5 from WT C57BL/6 females. Cortical tissue of each embryo was dissected on ice-cold Hank's Balanced Salt Solution (Gibco, 14170-112). Pooled tissue was minced and digested with 0.05% Trypsin-EDTA (Gibco, 25300-054) at 37°C for 12 min. Cells were triturated, resuspended in modified neurobasal media [Glutamax (Gibco, 35050-061), 2% penicillin/streptomycin (Gibco, 15140-122), and B27 (Gibco, 17504-044)], and seeded at 0.25 × 10E6 cells/well in 6-well plates pre-coated with poly-L-lysine (Sigma, P1274-500MG).

Neurons were treated with ASO doses on *in vitro* day 7 after culture and collected 7 days after treatment. The toxicity of each ASO was determined using the ApoTox-Glo triplex Assay (Promega, G6320) as per manufacturer instructions.

Stereotactic i.c.v. injections. For Pups (P1-2). Mouse pups were cryo anesthetized on ice on a cooled stage of a Digital Just for Mouse Stereotaxic Instrument (Stoelting, 51730D). The head of the anesthetized pup was securely placed flat between ear cups to ensure a level head position for injection. ASO (weight-based) or PBS (2μL) were loaded into a Hamilton 1700 syringe (Hamilton Company, CAL7635-01) with a 32-gauge, 0.5-inch needle (Hamilton Company, 7803-04) and secured by the Quintessential Stereotaxic Injector (QSI; Stoelting, 53311). The needle tip is aligned with the pups' lambda suture, which is visible through the skin in neonates. This lambda point was used as the reference point ("zero") to target the lateral ventricles: e.g., for right-sided injection; the syringe was moved to +1.50mm (anterior); -0.80mm (right); and -1.50mm (deep). Injections were pushed at a rate of 0.5μL/min. The needle was slowly retracted to avoid material leakage.

RNA extraction, qRT-PCR and Nanostring. To determine the expression of Tubb4a from mouse brain, tissues were dissected and snap frozen. RNA extraction, c-DNA, qRT-PCR and Nanostring details are provided in Supplemental Methods.

Histology. Mice were anesthetized and transcardially perfused with an initial flush of PBS (Thermo Scientific, 1001-023) followed by 4% paraformaldehyde (PFA). Anesthetic methods varied by age with isoflurane gas/oxygen flow for adolescent mice (>P8) or a weight-based injection of a xylazine, ketamine, and PBS mixture for adult mice (>P21). The harvested whole brain tissue was post-fixed with 4% PFA in PBS overnight at 4ºC, then rinsed in PBS and transferred to 30% sucrose in PBS at 4ºC until the sample was no longer buoyant (>3 days), indicating penetrance of the sucrose solution. The whole brain was then embedded in a Tissue-Tek Optimum Cutting Temperature compound (Sakura, 4583) and cryosectioned at 20μm by microtome (Leica, CM3050S) into coronal sections. These sections were stored in free-floating in PBS at 4ºC and transferred to a freezing medium comprised of a mixture of DMEM containing HEPES (Gibco, 11885084 and Sigma, H7523, respectively) and glycerol (Sigma, G6279-500) for long-term storage at -20ºC. For myelin staining, eriochrome Cyanine (Eri-C) staining was conducted using previously established methods (10). Sections were imaged by Leica

CTR6000/B microscope and Image J software was used to quantify myelin levels in the corpus callosum and cerebellum (10).

Immunofluorescence and image analysis. Brain sections were washed in PBS, blocked in 10% Normal Goat Serum (EMD Millipore, S26), 2% Bovine Serum Albumin (Sigma, A7030-100G), and 0.1% Triton X-100 (Sigma, T-9284) in PBS for 1 hour at room temperature (RT) and incubated in primary antibodies (See **Supplemental Table 5**) overnight at 4ºC. Following this incubation, sections were washed with 0.1% Triton X-100 (Sigma, T-9284) in PBS, incubated in fluorescent secondary antibodies for 1 hour, and protected from light at RT. In this study, AlexaFluor conjugated secondary antibodies were used at 1:1000 dilution. Sections were sequentially washed with 0.1% Triton X-100 (Sigma, T-9284) in PBS, and mounted onto Superfrost Plus Microscope Slides (Fisher, 12-550-15) using ProLong Gold Antifade Mountant with DAPI (ThermoFisher, P36931). Sections were imaged using a confocal microscope (Leica) or Keyence BZ-X810 microscope. Neurons (NeuN and/or CTIP2-labelled neurons) and OLs (ASPA+ or Olig2+) were quantified using ImageJ (FIJI) or Keyence BZ-X800 Analyzer software.

Electron microscopy. Mice were anesthetized with a weight-based injection of a xylazine, ketamine, and PBS mixture and transcardially perfused with an initial flush of PBS followed by a fixative solution composed of 2.5% glutaraldehyde, 2.0% paraformaldehyde in 0.1M sodium cacodylate buffer at pH 7.4. Optic nerve, corpus callosum, and cerebellar tissue were bluntly dissected and stored in the fixative solution. After overnight fixation at 4ºC, tissues were washed with buffer and post-fixed in 2.0% osmium tetroxide for 1 hour at RT. Tissue was then rinsed in dH2O before en-bloc staining with 2% uranyl acetate and dehydrated through graded ethanol. The tissue was embedded in EMbed-812 (Electron Microscopy Sciences), and thin sections were stained with uranyl acetate and lead citrate. Sections were examined with a JEOL 1010 electron microscope fitted with a Hamamatsu digital camera and AMT Advantage NanoSprint500 software. The images for EM sections were assessed using Image J software, and the inner and outer axonal area was measured for g-ratio analysis and quantified in 50 axons per animal with n = 3 per group.

RNAscope. Mouse brains were harvested by standard perfusion, including overnight post-fixation followed by 30% sucrose in PBS incubation for 3 days at 4ºC followed by paraffin embedding and sagittal sectioning. For Chromogenic InSitu Hybridization (CISH) staining, fresh slides were sectioned, air-dried, and baked within 48hrs of staining. Staining was performed on a Bond RXm

automated staining system (Leica Biosystems). For CISH probe staining, a Mm-Tubb4 probe (Advanced Cell Diagnostics, 590508) was used along with RNAscope 2.5 LSx Reagent Kit Red (Advanced Cell Diagnostics, 322750) using standardized protocols from Advanced Cell Diagnostics. After staining, slides were scanned at 40x magnification with an Aperio CS-O slide scanner (Leica Biosystems).

Immunoblotting. Brain tissues were dissected to protein levels in different regions of the brain (incl. cortex, striatum, and cerebellum) at different ages, and immunoblotting was performed as explained in Supplemental methods.

Behavioral Assays

The rotarod, tremor assay, grip strength, and open field were conducted as published previously (10, 33, 34). The Supplemental method section includes the methods of behavioral assays.

Electrode implantation surgeries, Evoked potential stimuli presentation and data analysis.

Electrode Implantation: Electrode implantation was performed (35, 36) under isoflurane anesthesia, consisting of stereotaxic placement of 10 electrodes (Hippocampal, bilateral barrel/parietal, bilateral motor, bilateral auditory, bilateral visual electrodes) using the following coordinates (From Bregma: Bilateral motor: 0.5mm Anterior–Posterior (A-P) and 1.0mm Medial–Lateral (M-L); bilateral barrel/parietal: -0.7mm A-P, 3.0mm M-L; bilateral auditory -2.7mm A-P and 4mm M-L; bilateral visual -3.6mm A-P, 2.3mm M-L; Hippocampus: – 2.2mm A–P, 2.0mm M–L and 1.7 mm ventral). The electrodes were produced by attaching 125uM silver wire for hippocampal leads (78600, A-M Systems) and 0.004 Inch (125um) silver wire for cortical leads (CFW0013001, California Fine Wire) attached to an 18-channel Omnetics nano connector (Omnetics, A79014-001). The electrodes were placed in the superficial cortical surface after drilling 1mm with a 0.35 Drill Bit (Lecia 39416021) holes at each stereotaxic location. The electrodes were covered with dental cement (Lang 1323CLR) which attached the connector to the head.

Evoked Visual and Auditory Stimuli: Animals were placed in custom-built cages and allowed to acclimate to the dark for 30 minutes prior to recording. The mice were presented with a 1Hz light flicker stimulus for 2 minutes generated by Arduino Uno Board connected to Atmel Atmega8/168/328 AVR microcontroller and FTDI FT232 breakout board (SparkFun Electronics).

Light intensity was measured with a light meter model 840006C (Sper Scientific). After a 5-minute rest period, the mice were presented with 82Db, 15ms white noise stimulation train for 17 minutes generated by WaveForm Generator model 2414A (Tegam). Decibels were measured from the center of four cages using Sound Meter App version 1.7.5 SM-J337P, US (Smart Tools Co.). The evoked potentials were recorded using the 32 channel Intan extracellular amplifier.

Analysis of Evoked Potentials: Raw EVP data was imported into MATLAB R2021b (Mathworks Inc., Natick, MA) via read_Intan Gui (Intan Technologies, Los Angeles, CA). The EEG and EVP data underwent artifact rejection algorithm removing signal with root mean square amplitude of >200 or <30 and skew >0.4. For auditory and visual potential analysis, the leads over auditory and visual cortex were averaged using in house written scripts in Matlab that averaged the signals based on a TTL pulse that was generated with each stimuli. The average stimuli were presented via a marking GUI in Matlab and a scorer marked regions around the N1, P1 and N2 peaks and the software chose the highest peak and measured amplitude and latency for both left and right auditory or visual channel for each mouse. The latencies were averaged for the left leads for both auditory and visual stimuli. For electrophysiology, the averaged latencies were plotted in MATLAB R2021b and statistical analysis was conducted.

Statistical analysis: All data are presented as the mean ± standard error mean (SEM) in figures. For mouse studies, 'n' represents the number of animals used per experiment unless indicated otherwise. Rotarod, tremor, and grip strength for the *Tubb4a*$^{D249N/KO}$ mouse model characterization and for ASO treatment were evaluated using mixed effects analysis. Likelihood ratio testing was used to determine model fit. Kaplan-Meier curves with log-rank testing were used to compare survival between groups. Median survival time is reported with 95% confidence intervals. Cox regression was used to evaluate the association of ASO treatment on hazard of survival within genotype. Graphical methods such as log-log curves and Schoenfeld goodness of fit testing were used to test the proportional hazards assumption. Hazard ratio(s) of the model are reported with 95% confidence intervals. Comparisons in myelin quantification, NeuN, ASPA, NG2, Olig2, Ki-67 and cleaved caspase three counts and fluorescent intensity were analyzed by ordinary two-way ANOVA with multiple comparisons post-hoc Tukey tests. EM analysis for g-ratio and % myelin analysis was conducted two-way ANOVA followed by post-hoc Tukey test. Dose-response curves were calculated by Motulsky (4-parametric logistic) non-linear regression and the effective dose at 50% with 95% confidence intervals are reported. All statistical analyses were

performed using Prism 7.0 (GraphPad Software) or R (version 4.4.0), with two-sided testing and an alpha level of 0.05 for statistical significance.

Table 1: Potential ASO candidates showing >90% Tubb4a downregulation via gymnosis on mouse cortical neurons.

qRT-PCR determined % Tubb4a downregulation, and values were provided as Mean±SEM. *Tubb4a* expression is normalized to *sfrs9*. n=3-4 replicates per each ASO. For no ASO controls (n=9-10 replicates) ***p<0.0001

ASO#	**0**	**1μM**	**5μM**	**Apotox assay**
No ASO	100.02±2.6	NA	NA	No apoptosis
ASO 6	NA	70.0±3.2***	95.4±1.6***	No apoptosis
ASO 7	NA	65.2±1.5***	85.7±1.4***	No apoptosis
ASO 8	NA	77.4±0.6***	95.0±1.5***	Highly apoptotic
ASO 7-2	NA	86.9±1.6***	97.3±1.0***	No apoptosis
ASO 7-3	NA	58.8±2.2***	96.2±0.7***	No apoptosis
ASO 8-2	NA	73.4±4.3***	94.5±4.7***	No apoptosis
ASO 8-3	NA	66.1±1.2***	87.0±2.7***	No apoptosis
ASO 18-1	NA	70.7±7.2***	87.1±6.3***	No apoptosis
ASO 18-2	NA	68.9±0.8***	98.3±0.2***	Highly apoptotic
ASO 18-3	NA	66.4±2.9***	85.8±4.8***	No apoptosis

Acknowledgements:

We would like to thank Dr. Judith B. Grinspan for providing hybridoma antibodies; Pathology cores at CHOP for technical support of RNAscope and Elena Lysenko from Dr. Beverely Davidson's lab at CHOP for technical support for tremor assay.

This study was supported by funds from Synaptix Bio company; Kamens Chair in Translational Neurotherapeutics; H-ABC Foundation UK; and Commonwealth Universal Research Enhancement Program (CURE) funding (SAP # 4100077047).

Author Contributions:

SS, JLH, and AV designed the study and drafted the manuscript. SS, JLH, PN, and AB conducted experiments and performed and analyzed data. SS and AV supervised, conceptualized, and

coordinated the study. ADA conducted Nanostring, and AT provided her expertise and data analysis for Nanostring. SW helped in the statistical analysis of the data. JLH conducted and analyzed data for *in vivo* electrophysiology; EDM provided his expertise. SS, JLH, PN, AT, EDM and AV wrote the manuscript.

Conflict of interests:

SS holds a patent for downregulation of TUBB4A. AA holds a patent for downregulation of TUBB4A and is currently an employee of Merck with no COI. EDM is PI and receives research support from the Clinical trial site for studies from Acadia Pharmaceuticals, Takeda Pharmaceuticals, Marinus Pharmaceuticals, Stoke Therapeutics, and UCB Pharmaceuticals (Zogenix Pharmaceuticals). EDM receives funding from NIH, Curaleaf Inc, Penn Orphan Disease Center. AV receives research funding from Takeda, Sanofi, Affinia, Orchard, Homology, Passage Bio, Biogen, Boehringer Ingelhiem, Eli Lilly, Sana, Ionis, Myrtelle, Orphan Disease Center, PMD Foundation, AGSAA, H-ABC Foundation, CURE MLD, NINDS, NCATS, NICHD. AV holds a patent for downregulation of TUBB4A and a license for the AGS severity scale. EDM has consultancy (income) from Novartis Pharma and Acadia Pharma.

References:

1. Simons C, Wolf NI, McNeil N, Caldovic L, Devaney JM, Takanohashi A, et al. A de novo mutation in the beta-tubulin gene TUBB4A results in the leukoencephalopathy hypomyelination with atrophy of the basal ganglia and cerebellum. *Am J Hum Genet.* 2013;92(5):767-73.
2. van der Knaap MS, Naidu S, Pouwels PJ, Bonavita S, van Coster R, Lagae L, et al. New syndrome characterized by hypomyelination with atrophy of the basal ganglia and cerebellum. *AJNR Am J Neuroradiol.* 2002;23(9):1466-74.
3. Hamilton EM, Polder E, Vanderver A, Naidu S, Schiffmann R, Fisher K, et al. Hypomyelination with atrophy of the basal ganglia and cerebellum: further delineation of the phenotype and genotype-phenotype correlation. *Brain.* 2014;137(Pt 7):1921-30.
4. Schmidt JL, Pizzino A, Nicholl J, Foley A, Wang Y, Rosenfeld JA, et al. Estimating the relative frequency of leukodystrophies and recommendations for carrier screening in the era of next-generation sequencing. *Am J Med Genet A.* 2020;182(8):1906-12.
5. Joyal KM, Michaud J, van der Knaap MS, Bugiani M, and Venkateswaran S. Severe TUBB4A-Related Hypomyelination With Atrophy of the Basal Ganglia and Cerebellum: Novel Neuropathological Findings. *J Neuropathol Exp Neurol.* 2019;78(1):3-9.
6. Leandro-Garcia LJ, Leskela S, Landa I, Montero-Conde C, Lopez-Jimenez E, Leton R, et al. Tumoral and tissue-specific expression of the major human beta-tubulin isotypes. *Cytoskeleton (Hoboken).* 2010;67(4):214-23.
7. Hersheson J, Mencacci NE, Davis M, MacDonald N, Trabzuni D, Ryten M, et al. Mutations in the autoregulatory domain of beta-tubulin 4a cause hereditary dystonia. *Ann Neurol.* 2013;73(4):546-53.

8. Weigel M, Wang L, and Fu MM. Microtubule organization and dynamics in oligodendrocytes, astrocytes, and microglia. *Dev Neurobiol.* 2021;81(3):310-20.
9. Dent EW, and Baas PW. Microtubules in neurons as information carriers. *J Neurochem.* 2014;129(2):235-9.
10. Sase S, Almad AA, Boecker CA, Guedes-Dias P, Li JJ, Takanohashi A, et al. TUBB4A mutations result in both glial and neuronal degeneration in an H-ABC leukodystrophy mouse model. *Elife.* 2020;9.
11. Krajka V, Vulinovic F, Genova M, Tanzer K, Jijumon AS, Bodakuntla S, et al. H-ABC- and dystonia-causing TUBB4A mutations show distinct pathogenic effects. *Sci Adv.* 2022;8(10):eabj9229.
12. Curiel J, Rodriguez Bey G, Takanohashi A, Bugiani M, Fu X, Wolf NI, et al. TUBB4A mutations result in specific neuronal and oligodendrocytic defects that closely match clinically distinct phenotypes. *Hum Mol Genet.* 2017;26(22):4506-18.
13. van der Knaap MS, Linnankivi T, Paetau A, Feigenbaum A, Wakusawa K, Haginoya K, et al. Hypomyelination with atrophy of the basal ganglia and cerebellum: follow-up and pathology. *Neurology.* 2007;69(2):166-71.
14. Fertuzinhos S, Legue E, Li D, and Liem KF, Jr. A dominant tubulin mutation causes cerebellar neurodegeneration in a genetic model of tubulinopathy. *Sci Adv.* 2022;8(7):eabf7262.
15. Duncan ID, Lunn KF, Holmgren B, Urba-Holmgren R, and Brignolo-Holmes L. The taiep rat: a myelin mutant with an associated oligodendrocyte microtubular defect. *J Neurocytol.* 1992;21(12):870-84.
16. Voit T, Topaloglu H, Straub V, Muntoni F, Deconinck N, Campion G, et al. Safety and efficacy of drisapersen for the treatment of Duchenne muscular dystrophy (DEMAND II): an exploratory, randomised, placebo-controlled phase 2 study. *Lancet Neurol.* 2014;13(10):987-96.
17. Finkel RS, Chiriboga CA, Vajsar J, Day JW, Montes J, De Vivo DC, et al. Treatment of infantile-onset spinal muscular atrophy with nusinersen: a phase 2, open-label, dose-escalation study. *Lancet.* 2016;388(10063):3017-26.
18. Lin M, Hu X, Chang S, Chang Y, Bian W, Hu R, et al. Advances of Antisense Oligonucleotide Technology in the Treatment of Hereditary Neurodegenerative Diseases. *Evid Based Complement Alternat Med.* 2021;2021:6678422.
19. Cercignani M, Giulietti G, Dowell NG, Gabel M, Broad R, Leigh PN, et al. Characterizing axonal myelination within the healthy population: a tract-by-tract mapping of effects of age and gender on the fiber g-ratio. *Neurobiol Aging.* 2017;49:109-18.
20. D'Angelo E. In: Manto M, Schmahmann JD, Rossi F, Gruol DL, and Koibuchi N eds. *Handbook of the Cerebellum and Cerebellar Disorders*. Dordrecht: Springer Netherlands; 2013:765-91.
21. Yager LM, Garcia AF, Wunsch AM, and Ferguson SM. The ins and outs of the striatum: role in drug addiction. *Neuroscience.* 2015;301:529-41.
22. Ramahi JS, and Solecki DJ. The PAR polarity complex and cerebellar granule neuron migration. *Adv Exp Med Biol.* 2014;800:113-31.
23. Ostergaard ME, De Hoyos CL, Wan WB, Shen W, Low A, Berdeja A, et al. Understanding the effect of controlling phosphorothioate chirality in the DNA gap on the potency and safety of gapmer antisense oligonucleotides. *Nucleic Acids Res.* 2020;48(4):1691-700.
24. Andersson P. In: Arechavala-Gomeza V, and Garanto A eds. *Antisense RNA Design, Delivery, and Analysis*. New York, NY: Springer US; 2022:355-70.
25. Hagedorn PH, Brown JM, Easton A, Pierdomenico M, Jones K, Olson RE, et al. Acute Neurotoxicity of Antisense Oligonucleotides After Intracerebroventricular Injection Into

Mouse Brain Can Be Predicted from Sequence Features. *Nucleic Acid Ther.* 2022;32(3):151-62.
26. Moser VC. Functional assays for neurotoxicity testing. *Toxicol Pathol.* 2011;39(1):36-45.
27. Patel H, Martinez P, Perkins A, Taylor X, Jury N, McKinzie D, et al. Pathological tau and reactive astrogliosis are associated with distinct functional deficits in a mouse model of tauopathy. *Neurobiol Aging.* 2022;109:52-63.
28. Farley BJ, Morozova E, Dion J, Wang B, Harvey BD, Gianni D, et al. Evoked potentials as a translatable biomarker to track functional remyelination. *Mol Cell Neurosci.* 2019;99:103393.
29. Ainger K, Avossa D, Diana AS, Barry C, Barbarese E, and Carson JH. Transport and localization elements in myelin basic protein mRNA. *J Cell Biol.* 1997;138(5):1077-87.
30. Allinquant B, Staugaitis SM, D'Urso D, and Colman DR. The ectopic expression of myelin basic protein isoforms in Shiverer oligodendrocytes: implications for myelinogenesis. *J Cell Biol.* 1991;113(2):393-403.
31. Lopez-Juarez A, Gonzalez-Vega A, Kleinert-Altamirano A, Piazza V, Garduno-Robles A, Alata M, et al. Auditory impairment in H-ABC tubulinopathy. *J Comp Neurol.* 2021;529(5):957-68.
32. Hetzler BE, and Zeisset HL. THIP, a selective gamma-aminobutyric acid receptor agonist, alters flash-evoked potentials in rats. *Pharmacol Biochem Behav.* 1997;58(4):923-32.
33. Eliason SL, Stein CS, Mao Q, Tecedor L, Ding SL, Gaines DM, et al. A knock-in reporter model of Batten disease. *J Neurosci.* 2007;27(37):9826-34.
34. Joseph DJ, Von Deimling M, Hasegawa Y, Cristancho AG, Ahrens-Nicklas RC, Rogers SL, et al. Postnatal Arx transcriptional activity regulates functional properties of PV interneurons. *iScience.* 2021;24(1):101999.
35. Saby JN, Peters SU, Roberts TPL, Nelson CA, and Marsh ED. Evoked Potentials and EEG Analysis in Rett Syndrome and Related Developmental Encephalopathies: Towards a Biomarker for Translational Research. *Front Integr Neurosci.* 2020;14:30.
36. Ahrens-Nicklas RC, Tecedor L, Hall AF, Lysenko E, Cohen AS, Davidson BL, et al. Neuronal network dysfunction precedes storage and neurodegeneration in a lysosomal storage disorder. *JCI Insight.* 2019;4(21).

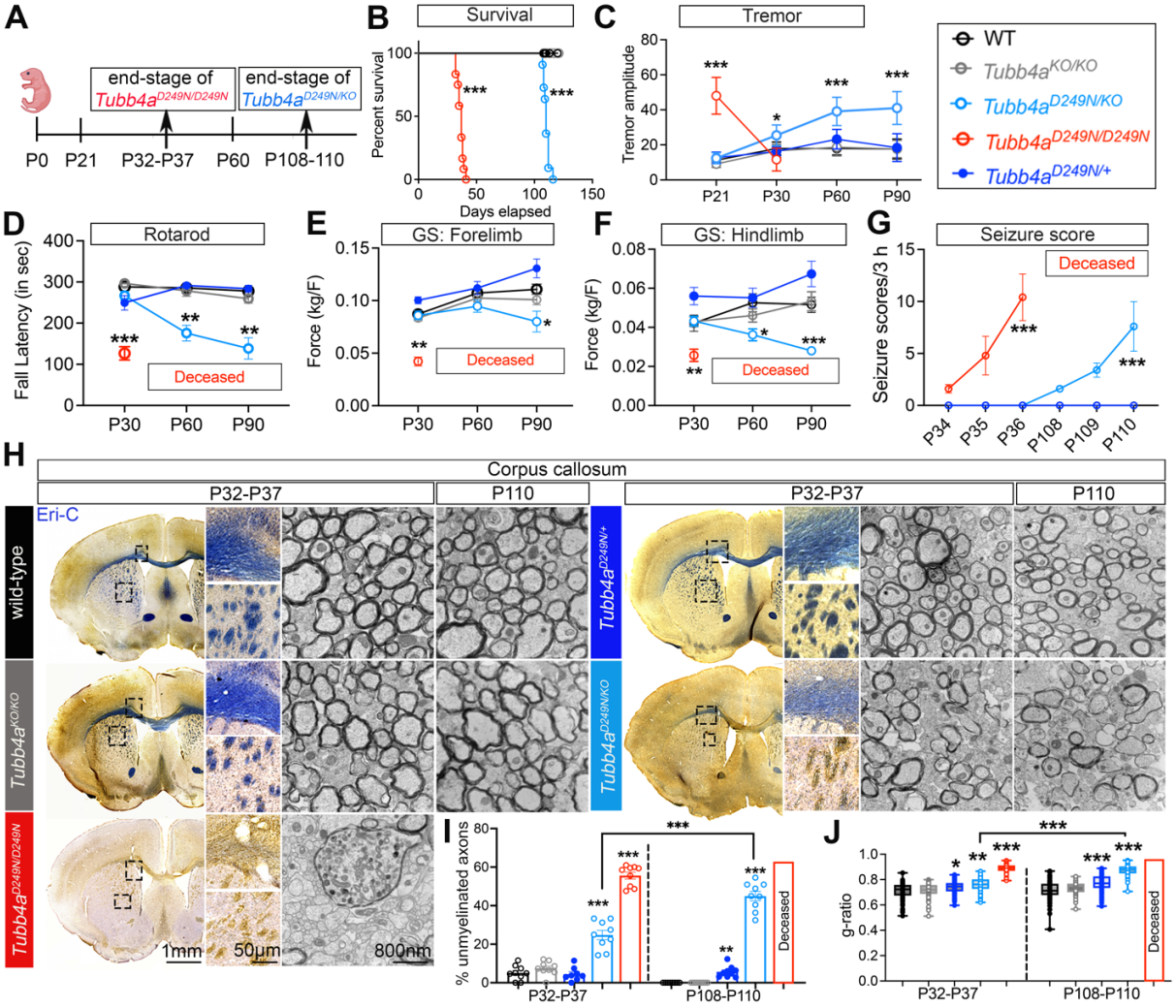

Figure 1: Tubb4a germline deletion is well-tolerated, and *Tubb4a*$^{D249N/KO}$ mice show severe H-ABC deficits. (A) Timeline schematics depicting the end-stages of H-ABC mouse models. Genotypes include WT, *Tubb4a*$^{KO/KO}$, *Tubb4a*$^{D249N/+}$, *Tubb4a*$^{D249N/KO}$, and *Tubb4a*$^{D249N/D249N}$. **(B)** Kaplan-Meier survival plot representing lifespans of all genotypes (n=11-15 per genotype). p-values calculated using log-rank test. **(C)** Graphical presentation of tremor amplitudes. n=12-15 animals per genotype. Performance of **(D)** Accelerating rotarod, **(E)** Forelimb grip strength (GS), **(F)** Hindlimb GS. n=6-15 mice per genotype and age. **(G)** Seizure counts of 3 hours. n=5 animals per genotype. p-values calculated using repeated measures post hoc two-way ANOVA compared to WT for behavioral tests. **(H)** Immunohistochemical images of myelin (Eriochrome cyanine [Eri-C]) staining and electron micrograph (EM) images of the corpus callosum at P32-P37 (end-stage of *Tubb4a*$^{D249N/D249N}$) and P108-P110 (end-stage of *Tubb4a*$^{D249N/KO}$). **(I)** Graphical presentation of % of unmyelinated axons at P32-P37 and P108-P110. n=3=4 animals per genotype and age. **(J)** Quantification of g-ratio at P32-P37 and P108-P110. n=3 animals per genotype, with 40-60 axons per animal. p-values are calculated using two-way ANOVA with Tukey corrections. *p<0.05, **p<0.001, ***P<0.0001. See long-term behavior in Supplemental Figure 1, Supplemental Figure 2-3 for Eri-C quantification, and Supplemental Figure 4 for optic nerve electron micrograph images and quantification.

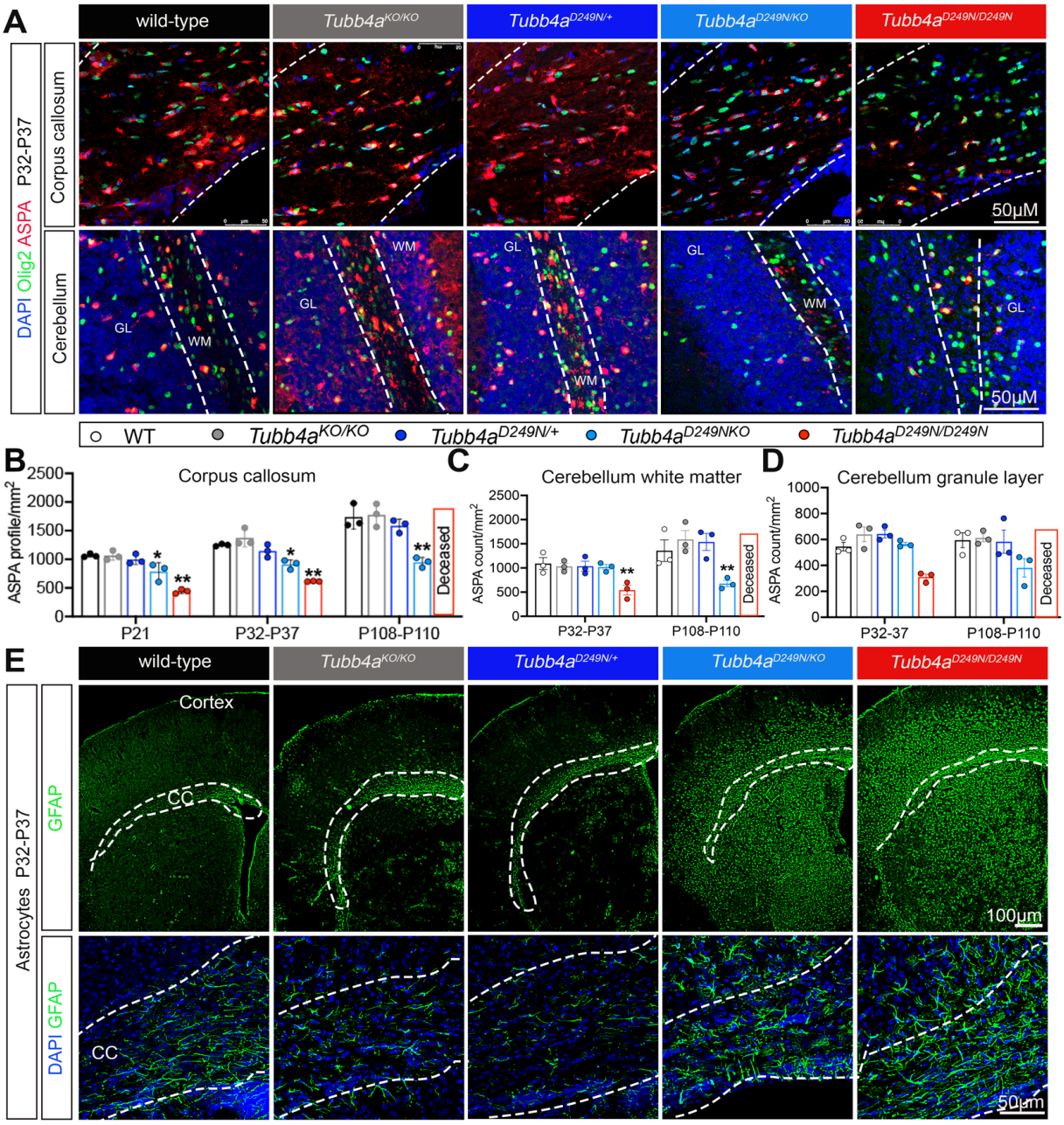

Figure 2: Germline suppression of mutant *Tubb4a* and relative preservation of WT *Tubb4a* rescues glial cell pathology. Groups include WT, *Tubb4a*$^{KO/KO}$, *Tubb4a*$^{D249N/+}$, *Tubb4a*$^{D249N/KO}$, and *Tubb4a*$^{D249N/D249N}$ **(A)** Immunohistochemical images of the corpus callosum and cerebellum at the P32-P37 showing Olig2 (oligodendrocyte lineage marker; green), and ASPA (mature oligodendrocyte marker; red) with DAPI (nucleic marker, blue). GL=granule layer; WM = white matter. **(B-D)** Quantification of ASPA counts per mm^2 in the corpus callosum (B), cerebellar white matter (C), and cerebellar granule layer (D). n=3-4 mice per genotype and age. **(E)** Immunohistochemical images of the corpus callosum at low (top panel) and high (bottom panel) magnification at the P32-P37 showing GFAP+ cells (green; astrocyte marker) and DAPI+ (blue). p-values for ASPA counts are calculated using two-way ANOVA with Tukey corrections. *p<0.05, **p<0.001, ***P<0.0001. Supplemental Figure 6 represents immunohistochemical images of ASPA+ Olig2+ cells at P108-P110 and Olig2 quantification at all ages. Other connected Supplemental Figures include Figures 7-9 (GFAP and Iba1 immunostaining).

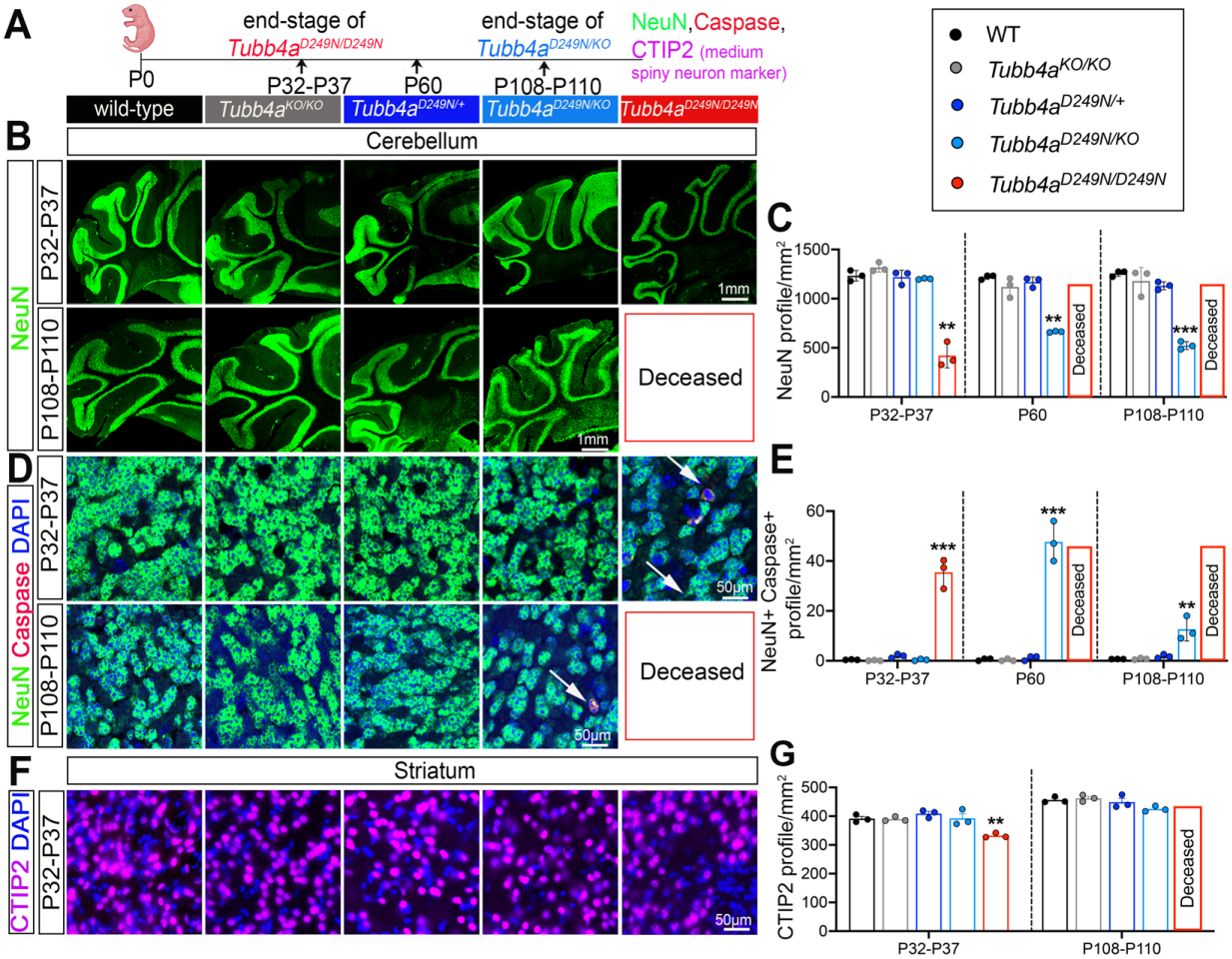

Figure 3: Germline suppression of mutant *Tubb4a* and relative preservation of WT rescues neuronal pathology. (A) Timeline schematic of humane endpoints for *Tubb4a* mouse models. Groups include WT, *Tubb4a*$^{KO/KO}$, *Tubb4a*$^{D249N/+}$, *Tubb4a*$^{D249N/KO}$, and *Tubb4a*$^{D249N/D249N}$. **(B)** Representative tiled images of NeuN immunostaining of cerebellar sections at the P32-P37 and P108-P110. **(C)** Graphical presentation of NeuN profiles per mm^2 at P32-37 (end-stage of *Tubb4a*$^{D249N/D249N}$), P60, and P108-P110 (end-stage of *Tubb4a*$^{D249N/KO}$). **(D)** Representative immunofluorescent images of cerebellum sections at high magnification at P32-P37 and P108-P110 that are stained with NeuN (green; neuronal marker), Caspase (red; apoptotic marker), and DAPI (nucleic marker). Arrows represent co-localized NeuN+ Caspase+ cells. **(E)** Graphical presentation of double-positive NeuN+ Caspase+ profiles per mm^2. **(F)** Representative images of striatum sections at the P32-37 stained with CTIP2 (magenta; medium spiny neuronal marker) and DAPI (blue, nucleic marker). **(G)** Graphical presentation of CTIP2 counts per field. n=3-4 animals are used per genotype and age. p-values are calculated using two-way ANOVA with Tukey corrections. *p<0.05, **p<0.001, ***p<0.0001. Associated Supplemental Figure 10 includes representative images of the P60 cerebellum and NeuN+ and CTIP2 profile in the striatum for other ages.

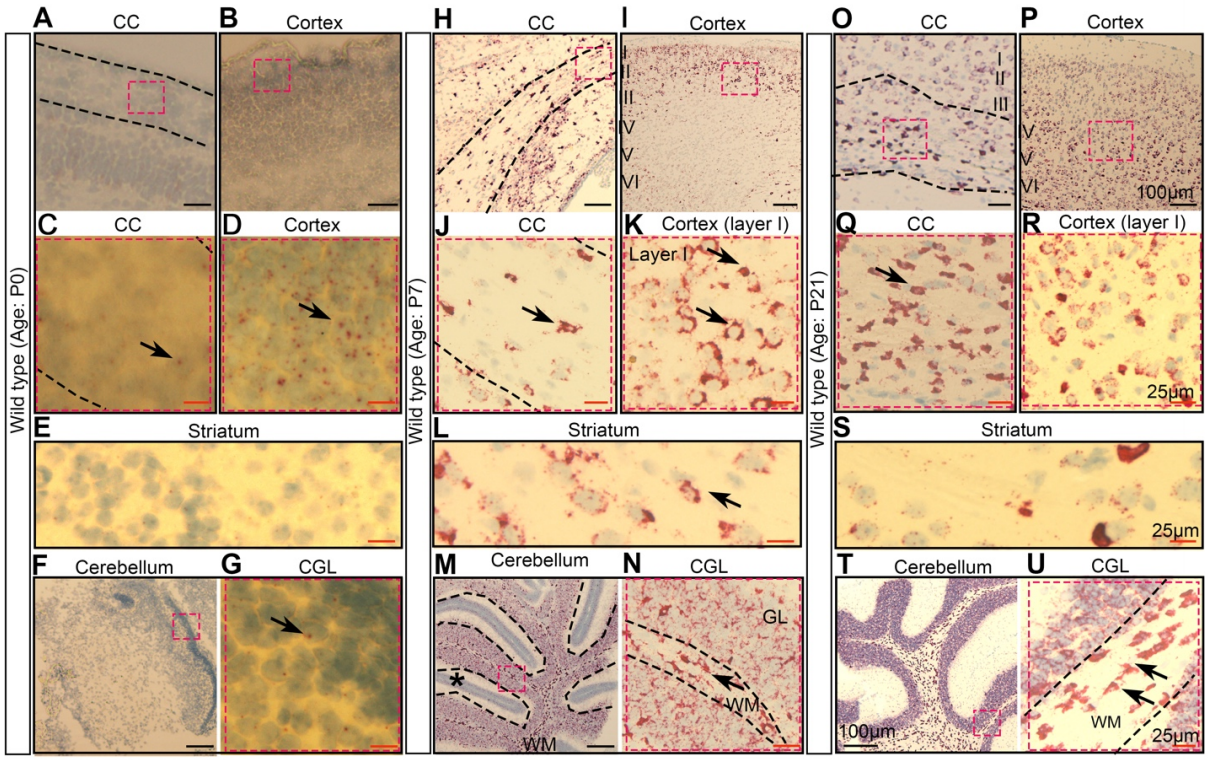

Figure 4: RNAscope in situ hybridization detecting Tubb4a transcripts at P0, P7, and P21 in WT sagittal brain sections. (**A-G**) Representative images of low [A-B, and F] and high [C-D, E and G] magnification Tubb4a RNAscope at P0 of the cortex, corpus callosum (CC), striatum and cerebellum. (**H-N**) Representative images of low [H-I, M] and high [J-K, L and N] magnification of RNAscope detecting *Tubb4a* transcripts at P7 of the cortex, CC, cerebellum, and striatum. (**O-U**) Representative images of low [O-P, T] and high [Q-R, S and U] magnification of RNAscope detecting *Tubb4a* transcripts at P21 of the cortex, CC, striatum and cerebellum. Arrows are used to denote a few *Tubb4a* transcripts. Tiled images of all corresponding ages are shown in Supplemental Figure 11. Supplemental Figure 12 provides Tubb4a RNAscope images at P14, P32-P35, and P108-P110.

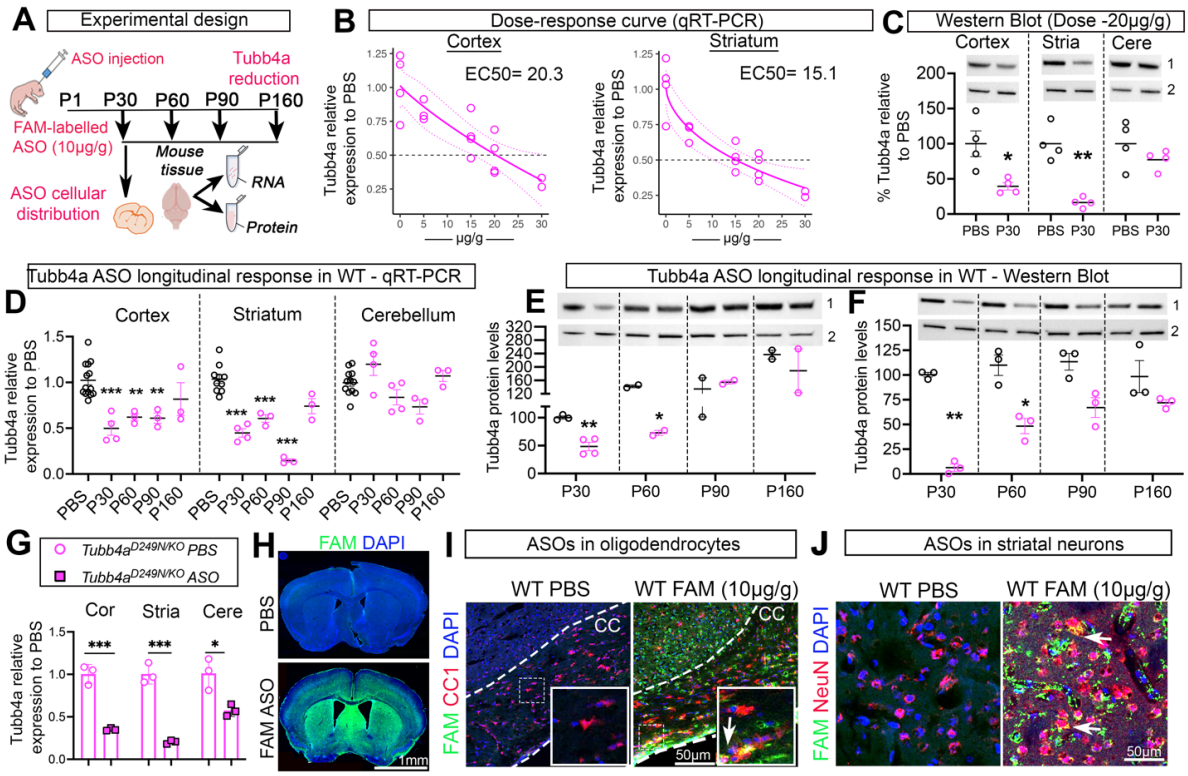

Figure 5: ASO 18-3 *in vivo* distribution in WT mice (A) Experimental design **(B)** Dose-dependent *Tubb4a* expression relative to PBS-injected controls at P30 in the cortex and striatum via qRT-PCR. **(C)** Western blot of Tubb4a protein at 20µg/g of ASO at P30 in the cortex, striatum, and cerebellum. 1=Tubb4a; 2=vinculin (housekeeping protein). n=3-4 WT mice are used for each dosage. **(D)** Longitudinal *Tubb4a* expression in WT mice was analyzed using qRT-PCR at 20µg/g of ASO 18-3 in different brain areas at P30, P60, P90, and P160. (**E-F**) Longitudinal Tubb4a protein levels in WT mice at P30, P60, P90, and P160 in the cortex (E) and striatum (F), 1=Tubb4a; 2=vinculin (housekeeping protein). n=3-4 WT mice are used for corresponding ages for Tubb4a expression. **(G)** Tubb4a expression via qRT-PCR in ASO-treated *Tubb4a*$^{D249N/KO}$ mice relative to PBS-treated *Tubb4a*$^{D249N/KO}$ mice at 20µg/g. For qRT-PCR, the *sfrs9* was used as a housekeeping gene to normalize the *Tubb4a* expression. For western blot, Tubb4a protein levels are normalized to vinculin. p-values are calculated using one-way or two-way ANOVA with Tukey corrections. *p<0.05, **p<0.001, ***P<0.0001. **(H)** Tiled images of coronal forebrain sections of DAPI (blue) and FAM (green). **(I)** Representative immunofluorescent images of the corpus callosum showing co-staining of CC1 (red; mature oligodendrocytes marker) with FAM (green) and DAPI (blue, nucleic marker). **(J)** Representative immunofluorescent images of the striatum region showing NeuN (red; neuronal marker) co-staining with FAM (green). Arrows represent co-localized signals. Associated Supplemental Figures include Supplemental Figures 13-21.

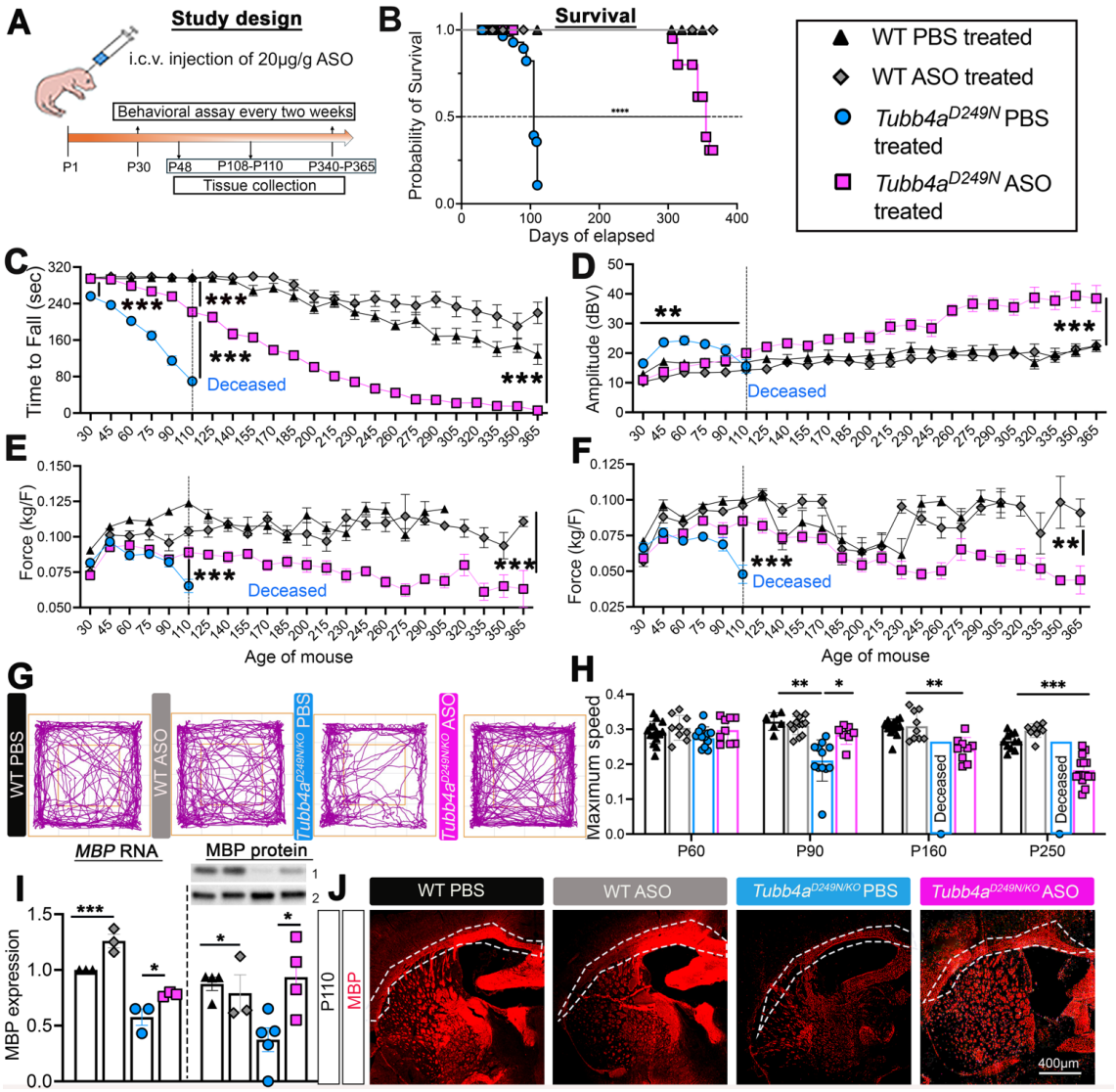

Figure 6 Survival, behavior, and myelin quantification in ASO-treated groups. Treatment groups include WT PBS, WT ASO, *Tubb4a*$^{D249N/KO}$ PBS-treated and *Tubb4a*$^{D249N/KO}$ ASO-treated. **(A)** Experimental design. **(B)** Kaplan-Meier survival analysis of different treatment groups with n=25-40 mice per group. p-values calculated using log-rank test. **(C)** Graphical presentation of accelerating rotarod test of treatment groups. **(D)** Graphical presentation of tremor amplitudes of treatment groups. (**E-F**) Graphical presentation of grip strength: Forelimb grip strength (E) and Hindlimb grip strength (F). n=20-25 mice were tested per group for rotarod, tremor assay, and grip strength. **(G)** Representative images of exploratory activity of open field at P90. **(H)** Graphical presentation of maximum speed of treatment groups. n=12-13 mice were tested per group. **(I)** Graphical presentation of quantification of *Mbp* transcripts (using Nanostring) and MBP western blot in the striatum at P48 (See Nanostring in Supplemental Figure 30). n=3 per treatment group for Nanostring and Western blotting. 1= MBP (Molecular weight-18kDa) and 2= GAPDH. GAPDH is used as a housekeeping protein to normalize MBP protein. **(J)** Representative immunofluorescent images of the forebrain section showing MBP staining (red) pattern across different treatment groups. For behavioral tests, p-values are calculated using repeated measures ANOVA with mixed effects analysis. *p<0.05, **p<0.001, ***P<0.0001. Associated Supplemental Figures include Supplemental Figure 22.

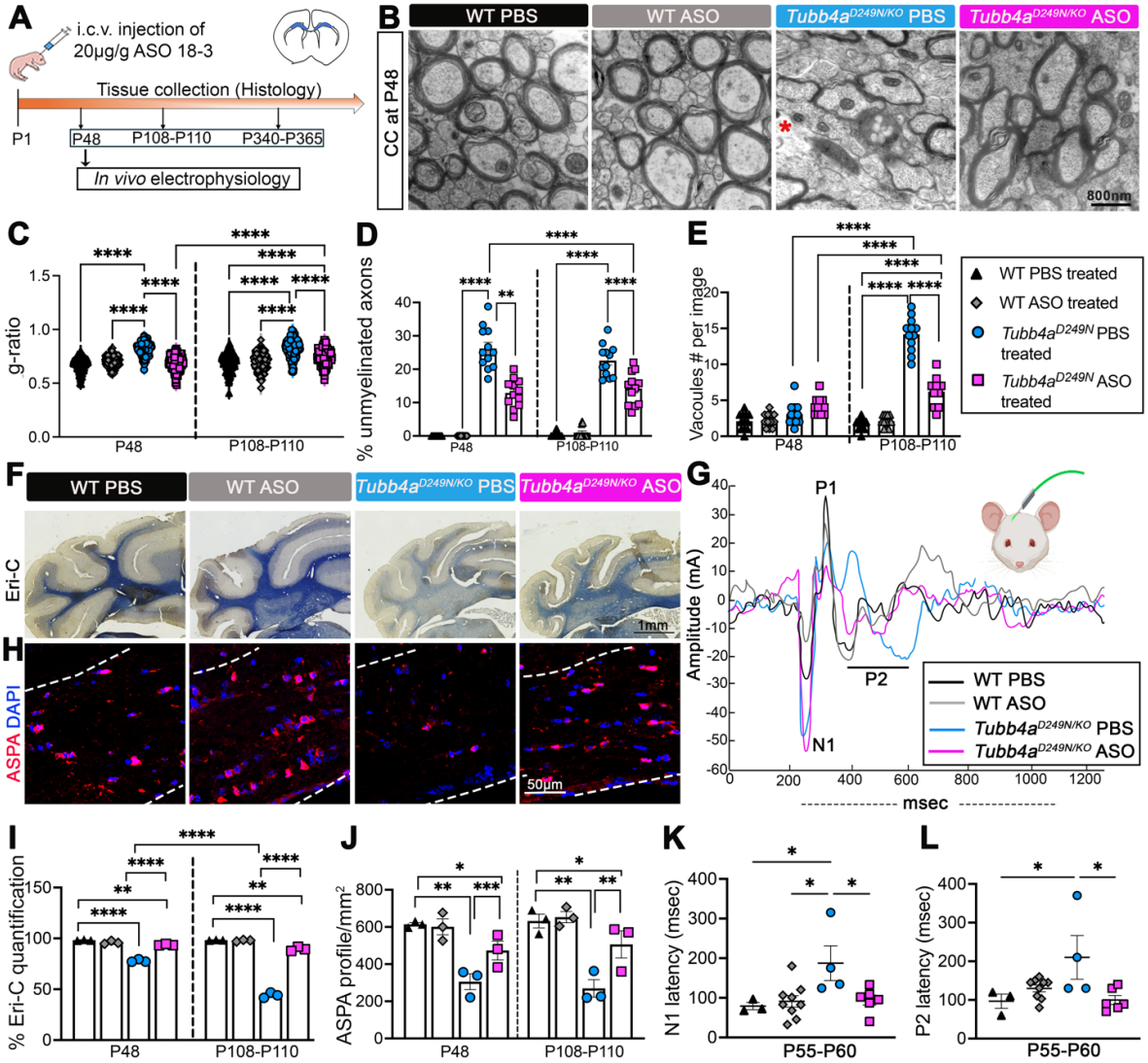

Figure 7 Neuropathological analysis in ASO-treated groups. Treatment groups include WT PBS, WT ASO, *Tubb4a*$^{D249N/KO}$ PBS-treated, and *Tubb4a*$^{D249N/KO}$ ASO-treated. **(A)** Study design **(B)** Representative EM images of ASO-treated mice of the corpus callosum at P48. **(C)** Graphical presentation of g-ratio across different treatment groups. **(D)** Graphical presentation of % unmyelinated axons across different treatment groups. **(E)** Graphical presentation of the number of vacuoles (Vacuoles #). For EM data, n=3-4 animals are used, and at least 4-5 images per animal are used. For the g-ratio, at least 30-40 axons per image were used to measure the g-ratio. **(F)** Representative histochemical images of Eri-C (myelin) staining in the cerebellum at P48. **(G)** The mean of visual evoked potential peaks of all groups generated using MATLAB. **(H)** Representative immunofluorescent images of ASPA+ (red) DAPI+ (blue) cells in the corpus callosum at P48 **(I)** Graphical presentation of myelin quantification (Eri-C) analysis across treatment groups. **(J)** Graphical presentation of ASPA+ Olig2+ cells in the corpus callosum. **(K and L)** Graphical presentation of N1 and P2 latencies at P48. n=3-9 animals per treatment group. p-values are calculated using one-way or two-way ANOVA with Tukey corrections. *p<0.05, **p<0.001, ***p<0.0001. Connected Supplemental Figures are Supplemental Figures 24-31.